Journal Name

ARTICLE TYPE

Cite this: DOI: 00.0000/xxxxxxxxxx

Floating catalyst carbon nanotube synthesis assisted by premixed hydrogen/air flames

Cen Zhang,*[a] Bo Tian,[a,b] Cheng Tung Chong,[c] Boning Ding,[d] Luming Fan,[a], Xin Chang,[a] and Simone Hochgreb[a]

Received Date
Accepted Date

DOI: 00.0000/xxxxxxxxxx

Carbon nanotubes (CNTs) were synthesised in the post flame region of premixed laminar flat H2/air flames using feedstocks containing ethanol and ferrocene. The as-produced nanomaterials were collected downstream of the post-flame region at a fixed height above burner of 230 mm and were characterised by various techniques including Raman spectroscopy, scanning electron microscopy and X-ray diffraction (XRD). A formation window of ϕ = 1.05–1.20 was identified, and the resulting flame temperatures were found to be the dominant limiting factor for producing CNTs. CNT bundles were formed and the diameter of individual CNTs were observed to be smaller than 5 nm. The formation of CNTs was accompanied by production of highly crystalline nanoparticles of a dimensions between 20 and 100 nm, which were identified as Fe_3O_4 by XRD.

1 Introduction

Carbon nanotubes (CNTs) were first discovered by Iijima in 1991 whilst using an arc discharge evaporation method for producing fullerene[1]. These hollow-shaped CNTs typically consist of a single or multiple walls of concentric graphene layers. The average diameter of a single-walled CNT (SWCNTs) is typically between 0.8-2.0 nm, while multi-walled carbon nanotubes (MWCNTs) can be orders of magnitude larger than SWCNTs depending on the number of walls[2]. Owing to their unique physical structures including curved graphitic layers and high aspect ratios, CNTs possess exceptional mechanical, thermal and electrical properties, and therefore are regarded as an advanced functional material. The past few decades have witnessed a rapid expansion of the research community for CNTs. Their applications include but are not limited to mechanically and electrically enhanced polymer composites[2–5], multi-functional coatings[6], ultrathin films[7] and electrode components[8].

The current mainstream methods for producing CNTs are plasma arc discharge (PAD), pulsed laser vaporisation (PLV) and chemical vapour deposition (CVD). The first two methods are common ways for producing highly crystalline CNTs on a limited scale, while CVD methods are popular tools for mass production of CNTs. There are a few CVD configurations including fixed beds[9], fluidised beds[10], floating catalysts[11], and many other combinations such as plasma-enhanced CVD methods[12]. Among these methods, floating catalyst CVD or FCCVD has attracted increasing attention by many researchers and industry due to its continuous, scalable and controllable production characteristics. Catalysts and carbon sources are initially vaporised and mixed in this method before driven into the hot reaction zone, which makes it possible to continuously produce CNTs in a large quantity.

Flame-assisted synthesis is already a well-known alternative technique for materials production, and responsible for the high throughput of many commercial products such as carbon black, fumed silica and titanium dioxide pigment are typically realised via this method[13]. Flame synthesis of CNTs was first reported by Howard *et.al* using premixed hydrocarbon/oxygen flames (C_2H_2, C_2H_4 and C_6H_6) at low pressures[14]. Since then, different flame configurations have been developed for producing CNTs, and comprehensive reviews are detailed in Ref.[15–17].

Unlike CVD methods which typically rely on furnaces, a flame synthesis setup uses heat from a flame through direct combustion of flammable mixtures. This method may be categorised into two main classes based on the types of flames in use: diffusion flames[18–20] and premixed flames[21–25]. In either case, an appropriate carbon source must be selected for the CNT production.During synthesis, elemental metal nanoparticles (typically Ni, Fe, Co, *etc.*) act as catalysts, over which the inception of the solid graphitic layers is initiated at high temperatures[15]. CNTs

[a] *Department of Engineering, University of Cambridge, Trumpington Street, Cambridge CB2 1PZ, United Kingdom. E-mail: cz299@alumni.cam.ac.uk*
[b] *College of Engineering and Technology, University of Derby, Markeaton Street, DE22 3AW, Derby, United Kingdom*
[c] *China-UK Low Carbon College, Shanghai Jiao Tong University, 800 Dong Chuan Road, Shanghai, China*
[d] *Department of Materials Science and Metallurgy, University of Cambridge, 27 Charles Babbage Road, Cambridge CB3 0FS, United Kingdom*

then grow upon the surfaces of the catalytically active nanoparticles, supported either by metal alloy substrates[22], or suspended as particles in the gas phase[25,26].

Diffusion flame systems have a variety of arrangements including co-flow[19,27,28], inverse[29] and counter-flow[20,30,31] configurations. These systems are favoured due to their ease of assembly and minimal risk of flashback characteristics. However, soot formation is a common problem for diffusion flames if hydrocarbons are used as the carbon source. Furthermore, CNTs must be extracted from the flame at a very early stage, as the catalytically active nanomaterials are otherwise deactivated by the rapid oxidation across the flame zone[29].

In contrast, premixed flames offer certain advantages relatively to their diffusion counterparts, in that the flame structure is one-dimensional and well characterised, with fixed equivalence ratios which determine the product temperature. Owing to these benefits, the characterisation of the synthesis process by numerical analysis such as thermodynamic equilibrium calculations becomes possible, which render the configurations as an attractive tool to unveil the underlying mechanisms of CNT synthesis[32]. On the other hand, premixed flames can only be stabilised at certain equivalence ratios, thus limiting the range of compositions that can be achieved.

The synthesis configurations can be categorised into two groups: floating catalyst and catalyst support[18,22,24,33] setups. The former has potential for large scale production of CNTs due to the absence of substrates compared with the latter. For the floating catalyst method, precursors and carbon sources are initially vapourised before delivery to the reaction zone, in a similar way to FCCVD in furnaces[11,34]. There are only a few of studies using the floating catalyst premixed flame method, most of which were conducted at low pressures. Diener *et al.*[21] tested different fuels (C_2H_2, C_2H_4 and C_6H_6) and catalyst metallocenes (Fe, Ni and Co) for CNT synthesis at 10 kPa. C_2H_2 and C_2H_4 flames were reported capable of producing SWCNTs with a small quantity of MWCNTs, at ϕ of 1.7–3.8; whereas C_6H_6/O_2 flames were found to be capable of producing impurity-filled MWCNTs–estimated as 10% of the overall solid carbon output–over the same equivalence range. Height *et al.*[25] further investigated CNT synthesis in premixed C_2H_2/O_2/15%Ar flames at 6.7 kPa using iron pentacarbonyl ($Fe(CO)_5$) vapour as the catalyst, at a feeding concentration of 6000 ± 500 ppm (by mole) for the synthesis. They identified a window of ϕ for CNT formation as 1.5–1.9 and the overall yield of nanotubes was estimated as 0.1 wt.% of carbon and 2.5 wt.% of iron. In addition, iron oxides, primarily Fe_2O_3, were identified, and they claimed the growth of CNTs was a result of the catalytic character of Fe_2O_3. More recently, however, there seems to be a consensus that the continued growth of CNTs is attributed to catalytic elemental metal nanoparticles rather than oxides[15,35,36]. This interpretation was backed by Wen *et al.*'s study[26] using the same experimental setup as Height *et al.*[25] with different premixed flame compositions–CH_4/O_2/15%Ar flame at 26 kPa. In that study, two types of iron nanoparticles during synthesis were determined by X-ray diffraction (XRD): iron oxides (Fe_3O_4 and Fe_2O_3) and elemental iron; and the latter was identified as the direct catalyst for the growth of CNTs rather than the former.

Rather directly burning catalyst precursors with combustible mixtures in flames, Vander Wal *et al.* created a configuration where the synthesis takes place via pyrolysis instead of complete combustion[37,38]. This setup consists of a McKenna burner with a central tube and a stainless steel tube which is placed a few millimetres above the burner. Ferrocene carried by different gas mixtures, $CO/H_2/He$ or $C_2H_2/H_2/He$, was injected through the central tube and then into the stainless tube, while C_2H_2/air premixed flames were stabilised on the burner plate surrounding the tube for heat generation. They found CO was more effective than C_2H_2 as the carbon source, as the latter promotes the formation of polycyclic aromatic hydrocarbons (PAHs). These species were detrimental to CNT formation owing to their high thermodynamic stability and the inherent resistance to catalytic cracking[38]. In addition, they suggested that an appropriate amount of H_2 in the synthesis might remove excess carbon coating on catalyst nanoparticles and hence help retain the activity of the catalytic sites for CNT growth[37].

To further extend our understanding of CNT synthesis via flame methods, a floating catalyst configuration similar to that proposed Vander Wal *et al.* is proposed. In this paper, we demonstrate a controlled way of producing CNTs using a background premixed H_2/air flames as the heat source for conversion. A parametric study of the various factors affecting the synthesis process was also carried out, including the role of ϕ, feedstock injection and carrier flow rates.

2 Experimental

The apparatus consists of a premixed flat flame burner, a flow supply system, and a sampling unit, as depicted in Fig. 1. Premixed H_2/air flames were stabilised on a sintered copper ring (outer diameter 50 mm). An alumina tube (Almath Crucibles Ltd., recrystallised alumina 99.7% purity) of 10 mm outer diameter and 6 mm inner diameter was installed at the the centre of the ring for injecting vaporised ethanol (carbon source) and ferrocene (iron precursor). The tube outlet was purposely placed 5 mm above the burner surface to prevent burnout of carbon sources and catalysts by flames. The reacting environment was enclosed by a clear fused quartz tube of 75 mm outer and 70 inner diameter (Robson Scientific, SiO_2 99.995%). All flames were operated at atmospheric pressure.

In order to avoid excessive oxidation of the carbon source and catalyst precursors, operating conditions were constrained to rich premixed regions where $\phi \geq 1.00$, from 1.00–1.50. While a tiny amount of CH_4 (~0.4 vol.%) was doped for helping visualise the hydrogen flame front as a safety precaution. The contribution of CH_4 to the calculations of ϕ of the flammable mixtures was taken into account.

The experiments initially used the proportions of ethanol and ferrocene that have been successfully applied in FCCVD processes[11,39–42]. The liquid feedstocks were injected by a syringe pump (World Precision Instruments) at a range of injection rates into a purpose-built atomiser fed by a stream of argon that carried the atomised feedstocks into a temperature-controlled heated pipeline before entering the alumina tube for the subsequent synthesis. The atomiser and the pipeline were heated and main-

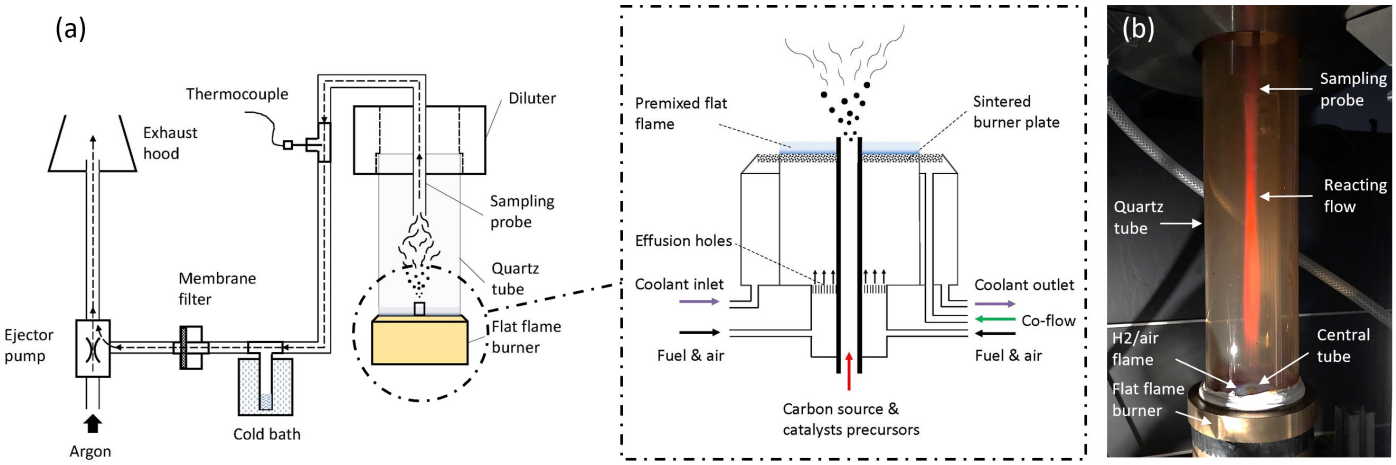

Fig. 1 Schematic of the experimental setup.

tained at 100 °C to ensure the liquid feedstocks could be fully vaporised. Ethanol (boiling temperature at 78.37 °C), thiophene (boiling temperature at 84 °C) and ferrocene (sublimation temperature $\geq$ 100 °C) were fully vaporised. The temperature of the vaporised feedstock and the carrier gas were *in situ* monitored by a thermocouple inserted inside the pipeline, just below the bottom of the burner, to ensure the injected feedstock was fully vaporised. The baseline feedstock used for the synthesis consisted of 99 wt.% ethanol and 1 wt.% ferrocene. If not explicitly stated otherwise, the feedstock injection rate and the flow rate of the argon flow used for carrying the vaporised reactants were set to 0.5 ml/min and 0.1 slpm, respectively. Accordingly, the mass flow rate of the gaseous feedstocks emerging from the central tube was 0.01 g/s, corresponding to a velocity of 0.27 m/s at the exit of the central tube given at a temperature of 100 °C. To achieve a precise regulation of all gas flows and catalysts, mass flow controllers (Alicat Scientific) were used in the system. Ethanol was chosen as the carbon source and the solvent for dissolving ferrocene and thiophene catalysts. N_2 was for diluting the post-flame products before discharging to the exhaust.

The synthesised materials were collected via a stainless steel probe (6 mm outer and 3 mm inner diameter) positioned at the height above burner (HAB) of 230 mm onto a PTFE membrane filter (SKC Ltd, pore size 0.45 μm). PTFE filters are chemically inert and hydrophobic, and therefore ideal for aerosol sampling in moisture-rich environments. The sampling flows were driven by an ejector pump (SMC ZH05L-X267) and further discharged to an exhaust. A cold finger device was designed to remove water vapour formed during the synthesis. This device consists of a tee pipe fitting with one port connected with a long stainless steel tube inserted into a cold bath filled with ice. This creates a localised cold site, which helps effectively condense and reduce water vapour from the sampling flow.

The as-produced samples collected on the PTFE filters were directly analysed by Raman spectroscopy (Horiba XploRA PLUS) in the range of 50–3000 cm^{-1} using a 532 nm wavelength laser. If not explicitly stated otherwise, 3 separate Raman spectroscopy measurements were carried out on each sample at random locations, which covered a spot with a diameter of roughly 1.2 μm) each. The obtained Raman spectra were then normalised against their respective global peak value before an averaged Raman spectrum for each sample was produced. The nanomaterials were further analysed by X-ray diffraction (Empyrean, Cu anode), scanning electron microscopy (Zeiss Leo Gemini 1530VP FEG-SEM) and transmission electron microscopy (FEI Tecnai Osiris FEGTEM).

3 Product gas temperatures

The expected state of the 1-D burner-stabilised flame was simulated using Cantera software. In the Cantera software tools, flames are assumed stabilised on a burner surface via heat transfer to the burner by conduction. The equations for mass, energy and species, along with the ideal gas state equation and chemical kinetic rates for the fuels used are solved. The resulting temperature is a function of the the boundary conditions provided by the mass flow rate, mixture composition and temperature of reactants. Details of the solution method are detailed in Ref.[43,44].

4 Results and discussion

4.1 Effect of temperature on the sample Raman spectrum

The temperature of the mixture is a critical parameter controlling the formation of nanomaterials.

Figure 2 shows the variation of calculated adiabatic (T_a) and burner stabilised (T_b) flame temperatures and mass fluxes ($\dot{m}''$) of the premixed H_2/air mixtures over equivalence ratios (ϕ from 1.00 to 1.50. The adiabatic temperature, T_a, peaks at ϕ=1.05, as determined by the maximum energy release per unit heat capacity of the equilibrium mixture. In contrast, the expected temperature above the burner, T_b, monotonically decreases from 1580 °C with increasing ϕ and reaches a plateau at around 1300 °C when ϕ gets to 1.3. In the present experiment, ϕ was varied by changing the air flow rate while keeping that of H_2 fixed at 7 slpm, which resulted in a decreasing $\dot{m}''$ with increasing ϕ (see Fig.2). Hence, the actual flame temperature T_b was significantly lower than its

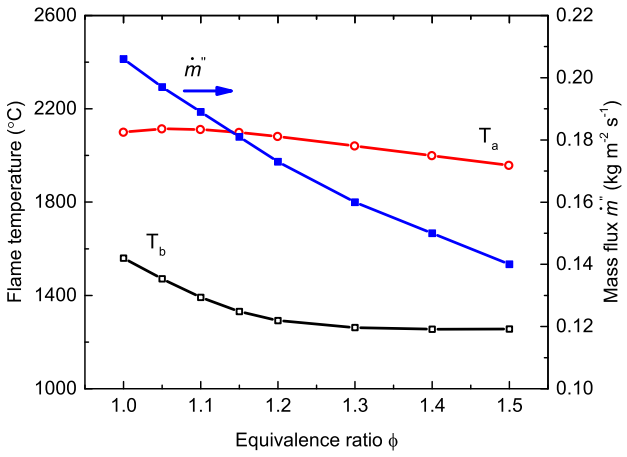

Fig. 2 Calculated adiabatic (T_a) and burner stabilised (T_b) flame temperatures and mass fluxes ($\dot{m}''$) of the premixed H_2/air mixtures as a function of equivalence ratios (ϕ). T_b were calculated based on a constant burner temperature of 25 °C and at atmospheric pressure.

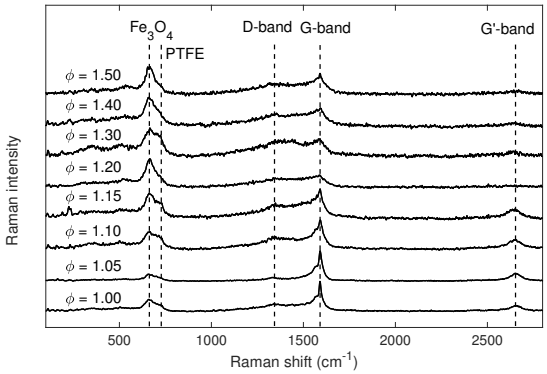

Fig. 3 Normalised Raman spectra of the samples produced at different equivalence ratios ϕ from 1.00 to 1.50. The feedstock consisted of 99.0 wt.% ethanol and 1.0 wt.% ferrocene, and was injected at 0.5 ml/min and carried by argon at 0.1 slpm.

adiabatic counterpart, primarily to the lower total heat release rate. Lower equivalence ratios were not used, as they were experimentally found to deliver lower CNT yields, as expected from an oxidising environment.

Figure 3 shows the average normalised Raman spectra of samples produced at the baseline condition over different ϕ from 1.00 to 1.50, corresponding to $\dot{m}''$ from 0.21 to 0.14 kg/m^2/s, and a calculated burned gas velocity of 1.21 to 1.07 m/s, respectively. Raman features of CNTs, G-band and a high intensity ratio of the G-band to D-band, I_G/I_D, are clearly seen between equivalence ratio of 1.00 and 1.15. The broad band at ~670 cm^{-1} is believed to be a feature peak of magnetite (Fe_3O_4)[45,46]; while a shoulder alongside this peak at 731 cm^{-1} is attributed to the background signal from the PTFE substrate. As ϕ increases, the CNT Raman features gradually fade away. In contrast, as ϕ approaches the stoichiometric point ($\phi = 1.00$), higher I_G/I_D ratios are achieved, compared with those at richer conditions. This implies a positive relationship between the yield of graphitic-CNTs at the highest synthesis temperatures.

A closer examination of the peak intensity ratio of the G-band to D-band, I_G/I_D, over different ϕ between 1.00 and 1.15 is illustrated in Fig.4. The I_G/I_D ratio at each ϕ is an average value taken from 12 Raman spectra in total obtained from two samples collected from two independent experiments. For each sample, 6 different Raman spectroscopy measurements were performed at random locations, and each covered a spot of a diameter of roughly 1.2 μm. Clearly, the I_G/I_D ratio decreases from 6.9 to 1.5 as ϕ increases from 1.00 to 1.15, which exhibits a positive correlation between T_b and I_G/I_D ratios, *i.e.* the higher the temperature the better quality of CNTs formed. Meanwhile the standard deviation decreases from 3.8 to 0.3 over the same region. The reason for change in unsteady deviation as ϕ approaches to 1.00 is unclear, but could be a result of in-sample different locations, or fluctuating temperatures and stoichiometries in the slowly flapping reacting zone as shown in Fig.1.(b). The later is evidenced by the observation when ϕ reaches 1.00 that the reddish flapping reaction zone switches to glowing yellow, indicating that ethanol from the central tube burns with excess oxygen due to fluctuating stoichiometries. Hence, the combustion of the ethanol vapour produces soot particles rather than graphitic materials, which is the likely cause of the large standard deviation in the Raman spectroscopy measurements.

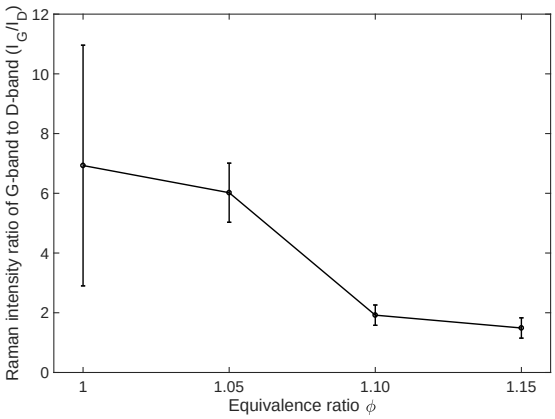

Fig. 4 Variation in peak intensity ratios of G-band to D-band for different ϕ from 1.0 to 1.15. The feedstock consisted of 99.0 wt.% ethanol and 1.0 wt.% ferrocene, and was injected at 0.5 ml/min and carried by argon at 0.1 slpm.

The combined results in Fig. 3 and 4 show that both flame temperature is a dominant parameter controlling the synthesis and quality of CNTs. Moreover, there exists an apparent minimum threshold temperature at ~1300 °C corresponding to $\phi = 1.20$, above which the Raman signatures of CNTs, G and D-bands, starts to emerge. This finding is in line with the results reported by FCCVD experiments, where the formation of SWCNTs and the same Raman signatures start to form beyond 1100 °C[11,34,47].

Figure 5 shows the average normalised Raman spectra of the G-band and D-band of the samples produced at ϕ from 1.00 to 1.15, which are deconvoluted into five Lorentzian peaks in the range of 1000–2000 cm^{-1} using a Gaussian-Lorentzian fitting function, a common algorithm applied for analysing Raman spectra

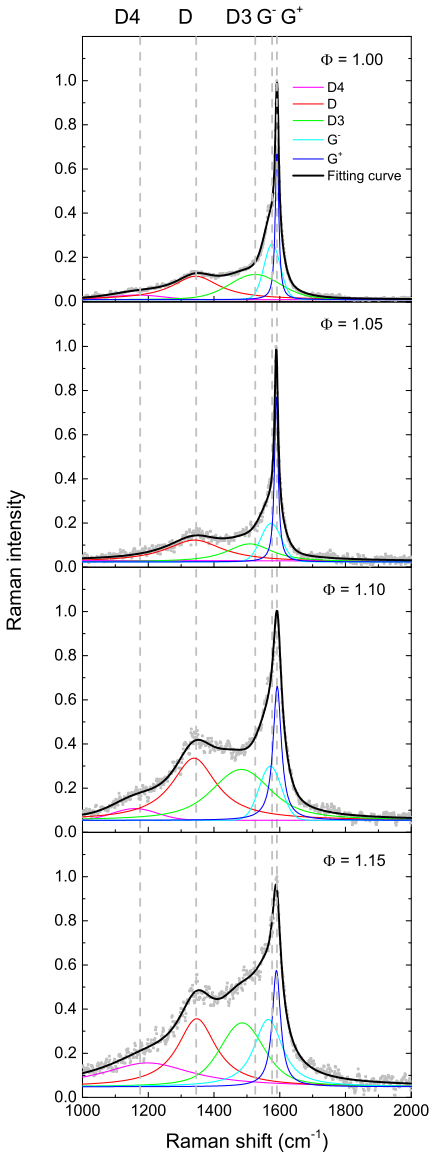

Fig. 5 Average normalised Raman spectra (shaded dot) and their spectral deconvolution into Lorentzian peaks in the wavenumber range from 1000 to 2000 cm^{-1} for ϕ from 1.00 to 1.15.

of CNTs[48]. The composite fitting curve, represented by the black thick line, can be fitted in an excellent agreement with the Raman spectra over different ϕ for all cases ((R^2 >0.98, where unity indicates a perfect fit). Specifically, the G-band comprises the G^- and G^+ components whereas the D-band comprises the D4, D, and D3 components. Compared with the G-band of graphite, which has only a single Lorentzian peak at 1582 cm^{-1}, the G-band of CNTs, particularly for SWCNTs, typically consists of both G^- and G^+ at 1570 cm^{-1} and 1590 cm^{-1}, respectively[49]. The G^+ feature is believed to be associated with the vibrations of carbon atoms in the direction of the axis of a CNT, the G^- feature, on the other hand, is a result of the vibration of carbon atoms along the circumferential direction of a CNT[49]. The Raman spectrum at $\phi = 1.05$ shows the highest G^+ peak (∼0.8) compared with the other conditions, decreasing as ϕ deviates from 1.05. Conversely, the normalised intensity of the G^- peak increases with ϕ deviating from 1.05, resulting in a decreased G^+/G^- intensity ratio. Based on Dresselhaus *et al.*'s findings, the relative intensity of G^+/G^- has a marked chirality dependence where semi-conducting CNTs have higher G^+/G^- values while those of metallic CNTs are close to unity[49]. However, this theory was built on the experimental study of isolated SWCNTs rather than bundles, hence, whether the theory still holds remains an open question, and a detailed investigation is needed.

The rise of the D-band of a CNT Raman spectrum is associated with defects or disorder in the materials, and its intensity is mainly a result of the D4, D, and D3 components at ∼1200 cm^{-1}, ∼1340 cm^{-1} and ∼1500 cm^{-1}, respectively[50]. The exact wavenumbers may deviate depending on the carbon structures of samples and the laser excitation wavelength. The D3 and D4 peaks can only be observed in soot or amorphous carbonaceous materials[50], whereas the D peak is widely seen in many carbon allotropes except for diamond. The rise of the D peak, as the most prominent peak in the D-band, attributes to the vibration of disordered graphitic lattice[50,51]. On the shoulder this peak, the D4 and D3 peaks are usually observed at lower and higher frequencies, respectively. The former is believed to be a result of the stretching vibrations of polyene-like structures and ionic impurities[51,52] while the latter has links with the amorphous contents presenting in soot such as organic molecules and fragments[50,52]. Generally, the normalised intensity of the D-band comprising all the three featured peaks increases as ϕ departs from 1.05, indicating a inversely proportional relationship with temperature. While that of the D4 peak keeps increasing as ϕ increases, in contrast to the other D peaks, which may indicate an increased proportion of polyene-like structures and ionic impurities formed in the materials.

Figure 6 shows the morphology and structure of nanomaterials synthesised at ϕ from 1.00 to 1.20 using the baseline feedstock. From Fig. 6.(a), the majority of the products consist of crystalline nanoparticles of characteristic size of 20–100 nm. Different shapes of nanoparticles are observed, including pyramid, sphere, cube and diamond. At ϕ=1.00–1.15, CNTs are loosely distributed and attached to the nanoparticles, as indicated by the arrows, tending to form a filamentous or web-like morphology. As ϕ increases to 1.2 and beyond, one starts to observe aggregates or lumps of nanoparticles, exhibiting a fundamentally different morphology. This implies a highly limited quantity of CNTs produced at this condition. The TEM image of CNTs products at ϕ of 1.05 suggests that the as-produced CNTs were inclined to form bundles with a diameter of the order of 10 nm and a length ranging from 100 nm up to 1 μm. Further, the diameter of the constituent individual CNTs was measured to be around 1 nm, implying the CNTs were single-walled.

XRD analysis was applied to investigate the identity of the crystalline nanoparticles. Illustrated in Fig.7 are the XRD patterns of Fe_3O_4, PTFE substrate and the synthesis materials produced at $\phi = 1.05$. The results, together with the featured Raman peak at around 670 cm^{-1} shown in Fig.3, confirms the crystalline nanoparticles consist primarily of Fe_3O_4, to which the CNT fibres are attached.

The mass flux $\dot{m}''$ of the H_2/air mixtures directly affects the

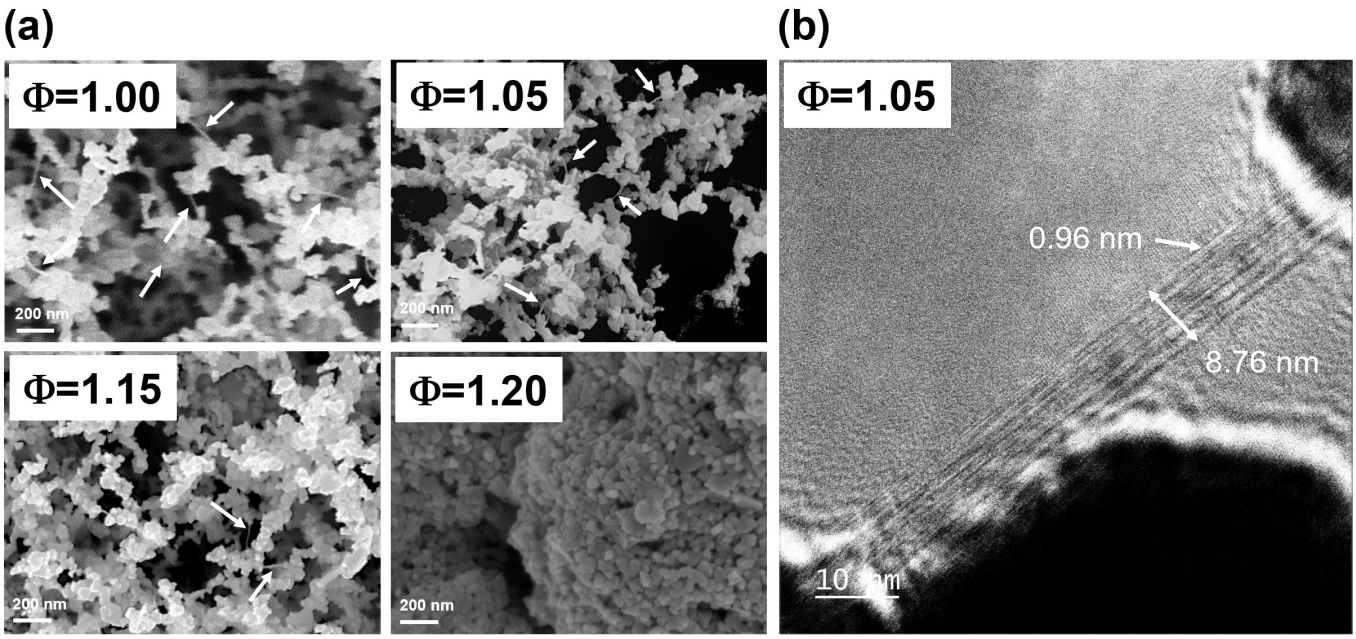

Fig. 6 Morphology and structure of the samples produced from the experiments. (a) SEM images of the as-produced nanomaterials at ϕ from 1.00 to 1.20 and (b) TEM image of SWCNTs produced at $\phi = 1.05$.

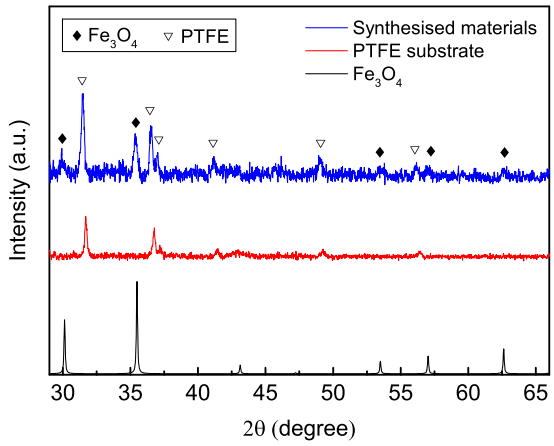

Fig. 7 XRD pattern of Fe_3O_4, PTFE substrate and nanomaterials produced at $\phi = 1.05$ using the baseline feedstock.

synthesis process at a fixed equivalence ratio. Higher mass fluxes rates lead to higher rates of heat release relatively to the heat loss, leading to higher temperatures (Fig. 8b) . We investigated this parameter by varying $\dot{m}''$ at the fixed equivalence ratio $\phi = 1.05$. Test 1 corresponds to a baseline case at $\dot{m}'' = 0.1$ kg m^{-}2 s^{-1} (3.5 slpm H_2 and 8.4 slpm air), whereas Test 2–4 were taken at 1.5, 2 and 3 times the mass flow rate of Test 1, respectively. The feedstock consisted of a fixed reactant flow of 99.0 wt.% ethanol and 1.0 wt.% ferrocene, and was injected at 0.5 ml/min and carried by argon at 0.1 slpm.

Figure 8(a) shows the normalised Raman spectra of the as-produced samples at Test 1–4. The Raman signals become sharper and more distinct with the increase in mass flux $\dot{m}''$. For the low mass flux case Test 1, neither the G-band (~1590 cm^{-1}) nor the D-band (~1350 cm^{-1}) are clearly identified, a sign of low yield of graphitic products. As $\dot{m}''$ increases, the featured peak at 731 cm^{-1} originating from the PTFE substrate diminishes, suggesting an increased yield of nanomaterials. It is worth noting that the radial breathing mode (RBM)–a unique Raman signature of CNTs as a result of the coherent radial vibration of C atom at frequencies of 120–350 cm^{-1} [49]–is captured by Raman spectroscopy as shown on the spectra of Test 2–4. Meanwhile, other Raman features of CNTs, the G-band, D-band and G'-band, also show up. Apparently, higher $\dot{m}''$ favours the formation of CNTs rather than the opposite, and it is evidenced by the drastic elevation of the I_G/I_D ratio which increases from 0.98 to 10.0 as $\dot{m}''$ changes from 0.1 to 0.3 kg m^{-2}s^{-1}. Again, the calculated T_b suggests that the threshold temperature for CNT formation is around 1300 ◦C, which agrees with the findings highlighted in Fig. 2.

A detailed examination of the material morphologies for different $\dot{m}''$ from Test 2 to 4 was conducted by SEM as shown in Fig. 8.(c). The figure illustrates the evolution of morphology of the nanomaterials as $\dot{m}''$ increases. The morphology for Test 1 is very similar to that of Test 2, and is therefore not included in the figure. For Test 2, only densely-packed solid nanoparticles were observed by SEM rather than CNTs, although some CNT fibres might be embedded beneath the nanoparticles as indicated by the Raman spectrum. As the mass fluxes (and corresponding temperatures) increased, corresponding to Test 3 and 4, CNTs formed a filamentous framework with crystalline nanoparticles attached (Fig.6). This type of arrangement implies an increased yield of CNTs, and an enhanced number density of CNTs to nanoparticles. More specifically, CNTs are more easily observed in Test 4 than

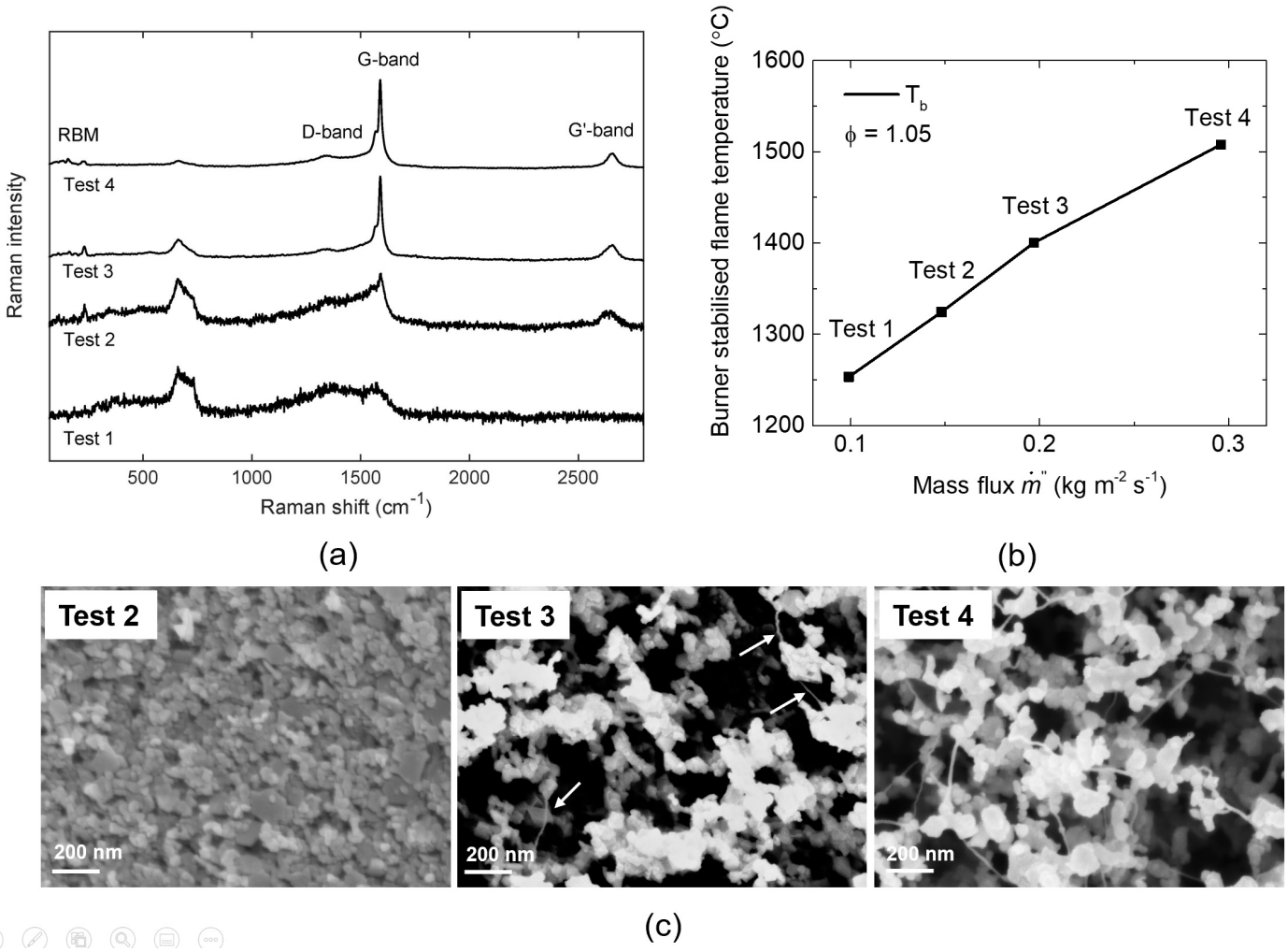

Fig. 8 (a). Normalised Raman spectra of the nanomaterials produced at $\phi = 1.05$ over different $\dot{m}''$ (0.1, 0.15, 0.2, and 0.3 kg m^{-2}s^{-1} corresponding to Tests 1–4, respectively). (b). Variation of calculated burner stabilised flame temperature T_b as a function of $\dot{m}''$ (at atmospheric pressure and at an inlet temperature of 25 °C). (c). SEM images of the nanomaterials collected at Test 2–4. The feedstock consisted of 99.0 wt.% ethanol and 1.0 wt.% ferrocene, and was injected at 0.5 ml/min and carried by argon at 0.1 slpm. Arrows indicate location of filamentous CNT.

any other conditions, due to a larger quantity and longer lengths of the CNT materials.

4.2 Effect of reactant injection rate

The rate of injection of the centrally injected reactants $\dot{q}$ and the carrier gas flow rate $\dot{V}_{Ar}$ were investigated in the following experiments.

The background burned air conditions of the were fixed at $\phi = 1.05$ (7 slpm H_2 and 16.7 slpm air), which yielded a calculated synthesis temperature of 1450 °C, leading to a expected burned gas velocity u_b of 57.3 cm/s. The effect of $\dot{V}_{Ar}$ was first examined by varying its value from 0.05 to 1.0 slpm, whilst keeping $\dot{q}$ fixed at 0.5 ml/min. Figure9(a) shows the average normalised Raman spectra of nanomaterials synthesised at different $\dot{V}_{Ar}$. In general, the variation of $\dot{V}_{Ar}$ shows little effect on the CNT synthesis up to 0.5 slpm, corresponding to a flow velocity of 64.0 cm/s comparable to that of the surrounding burnt gas flow of 57.3 cm/s. These Raman spectra exhibit a similar pattern as the Raman features of CNTs previously observed near the stoichiometric ratio, and the associated I_G/I_D ratios are all at around 5.0, suggesting a production of high quality CNTs. In contrast, when $\dot{V}_{Ar}$ reaches 1.0 slpm , at an estimated flow velocity equivalent to twice the value of the surrounding hot gases, the synthesised materials shows a much poorer Raman spectrum, indicating a decreased yield of CNTs and an increased proportion of amorphous carbon solids. This behaviour shows that for low values of the central gas velocity, CNT formation is controlled by the diffusion of heat, and corresponding reaction between the central reactants, heated by the surrounding gases. Beyond a certain inlet flow rate, however, heat diffusion through the reactant layer is insufficiently fast, and the inner reactant core leaves the system unreacted.

The reactant injection rate $\dot{q}$ was varied from 0.1 to 2.0 ml/min for a constant carrier flow rate $\dot{V}_{Ar}$ of 0.1 slpm, thus increasing the concentration of reactants by a factor of 20. The average normalised Raman spectra of the nanomaterials produced are shown in Fig.9(b). Generally, the G-band and the RBM can be observed for all $\dot{q}$, except for the lowest flow rates of 0.1 ml/min where no Raman features of CNTs are discerned, for which only

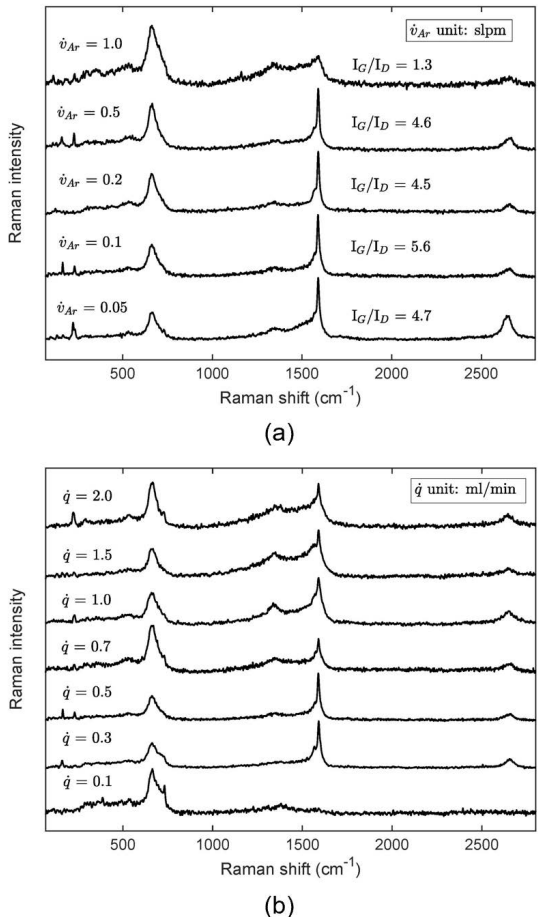

Fig. 9 Average normalised Raman spectra of the samples produced at $\phi = 1.05$ as a function of (a) different injection rates $\dot{q}$ from 0.1 to 2.0 ml/min, and (b) different argon flow rates $\dot{V}_{Ar}$ from 0.05 to 1.0 slpm.

Fe_3O_4 nanoparticles are detected by Raman spectroscopy, as the concentration of carbon source precursors are too low. As $\dot{q}$ increases beyond 0.1 ml/min, it is found that an optimum condition is reached, at which the Raman spectrum exhibits the most distinct features for $\dot{q}$ from 0.3 to 0.5 ml/min. Beyond 0.5 ml/min, the Raman spectra exhibit a broadened G-band and an enhanced D-band for all the conditions considered. The broadening effect appears due to the rise of the D3 peak, which is linked with amorphous species such as organic molecules or fragments[50,52] as discussed in the previous section. A drop in I_G/I_D ratios signals a decreased yield of CNTs for higher $\dot{q}$. The behaviour suggests that there is a minimum reactant concentration for the formation of CNTs, and that at some critical concentration, it is no longer the limiting factor for their formation. Beyond a certain concentration, the rate of heat diffusion into the central reactant column becomes rate limiting, so that higher concentrations just lead to poorer quality CNTs, and converstion into alternative products.

5 Conclusion

In this study, we have successfully demonstrated the feasibility of using a H_2/air background premixed flame to continuously produce CNTs using ethanol and ferrocene. The results are summarised as follows:

1. The temperature and stoichiometry of the surrounding gases is key to successful CNT synthesis, and operating at equivalence ratios just rich of the stoichiometry point is recommended. Rich operation ($\phi > 1.00$) is more favourable for producing CNTs, as no oxygen is left in the pyrolysis zone, avoiding rapid oxidation of the catalyst nanoparticles.

2. SWCNTs form as nanometer-thick fibrelets connecting the surrounding Fe_3O_4 crystals formed.

3. Higher mass fluxes of the surrounding burned gases lead to higher heat release per unit heat loss, and thus higher temperatures. This contributes to higher quantities, length and quality of CNTs formed.

4. There is an optimal range of both carrier flow rate and reactant concentration which maximises the quantity and quality of CNTs sampled. The results seem to indicate that there the limiting factor is the rate of diffusive heating of the reactants by the surrounding gases: beyond a limiting reactant gas or concentration flow rate, the heat cannot be transferred fast enough, and the CNT product quantity and quality degrades.

The present method is promising and inexpensive means of for CNT generation , particularly if the catalyst is chosen to be a desirable part of the product, for example oxide particles connected to CNTs for electrodes. However, significant work is required to better quantify the product yield. A detailed study of the effect of various ferrocene proportions in ethanol and the role of thiophene on the CNT synthesis has been carried out and is to be published in a future work.

Conflicts of interest

There are no conflicts to declare.

Acknowledgements

Cen Zhang thanks the China Scholarship Council and the Cambridge Trust for their financial support towards this research work. The overall project is funded under EPSRC UK Award EP/M015211/1 for the ANAM Initiative. The authors thank Dr Xiao Zhang and Dr Yanting Jin for their help with Raman and XRD analysis. The authors are also grateful to Dr Adam Boies and Prof Alan Windle for helpful discussions.

Notes and references

1 S. Iijima, *nature*, 1991, **354**, 56–58.
2 M. F. L. D. Volder, S. H. Tawfick, R. H. Baughman and A. Hart, *Science*, 2013, **535**, 535–540.
3 R. H. Baughman, Z. Anvar A. and W. A. de Heer, *Science*, 2002, **297**, 787.
4 R. Mora, J. Vilatela and A. Windle, *Composites Science and Technology*, 2009, **69**, 1558–1563.
5 J. Suhr, N. Koratkar, P. Keblinski and P. Ajayan, *Nature Materials*, 2005, **4**, 134–137.

6 A. Beigbeder, P. Degee, S. L. Conlan, R. J. Mutton, A. S. Clare, M. E. Pettitt, M. E. Callow, J. A. Callow and P. Dubois, *Biofouling*, 2008, **24**, 291–302.

7 Z. Wu, Z. Chen, X. Du, J. M. Logan, J. Sippel, M. Nikolou, K. Kamaras, J. R. Reynolds, D. B. Tanner, A. F. Hebard and A. G. Rinzler, *Science*, 2004, **305**, 1–3.

8 G. Lota, K. Fic and E. Frackowiak, *Energy and Environmental Science*, 2011, **4**, 1592–1605.

9 J.-F. Colomer, C. Stephan, S. Lefrant, G. Van Tendeloo, I. Willems, Z. Kónya, A. Fonseca, C. Laurent and J. Nagy, *Chemical Physics Letters*, 2000, **317**, 83–89.

10 F. Danafar, A. Fakhru'l-Razi, M. A. M. Salleh and D. R. A. Biak, *Chemical Engineering Journal*, 2009, **155**, 37–48.

11 Y.-L. Li, I. A. Kinloch and A. H. Windle, *Science (New York, N.Y.)*, 2004, **304**, 276–8.

12 K. B. Teo, S. B. Lee, M. Chhowalla, V. Semet, V. T. Binh, O. Groening, M. Castignolles, A. Loiseau, G. Pirio, P. Legagneux, D. Pribat, D. G. Hasko, H. Ahmed, G. A. Amaratunga and W. I. Milne, *Nanotechnology*, 2003, **14**, 204–211.

13 W. Y. Teoh, R. Amal and L. Mädler, *Nanoscale*, 2010, **2**, 1324–1347.

14 J. Howard, K. Chowdhury and J. Sande, *Nature*, 1994, 603.

15 W. Merchan-Merchan, A. V. Saveliev, L. Kennedy and W. C. Jimenez, *Progress in Energy and Combustion Science*, 2010, **36**, 696–727.

16 S. Li, Y. Ren, P. Biswas and S. D. Tse, *Progress in Energy and Combustion Science*, 2016, **55**, 1–59.

17 N. Hamzah, M. F. Yasin, M. Z. Yusop, A. Saat and N. A. Subha, *Journal of Materials Chemistry A*, 2017, **5**, 25144–25170.

18 R. L. Vander Wal, L. J. Hall and G. M. Berger, *The Journal of Physical Chemistry B*, 2002, **106**, 13122–13132.

19 L. Yuan, K. Saito, C. Pan, F. Williams and A. Gordon, *Chemical Physics Letters*, 2001, **340**, 237–241.

20 W. Merchan-Merchan and A. Saveliev, *Chemical Physics Letters*, 2002, **354**, 20–24.

21 M. D. Diener, N. Nichelson and J. M. Alford, *The Journal of Physical Chemistry B*, 2000, **104**, 9615–9620.

22 R. L. Vander Wal, L. J. Hall and G. M. Berger, *Proceedings of the Combustion Institute*, 2002, **29**, 1079–1085.

23 R. V. Wal and L. Hall, *Chemical Physics Letters*, 2001, **349**, 178–184.

24 R. Vander Wal, *Carbon*, 2002, **40**, 2101–2107.

25 M. J. Height, J. B. Howard, J. W. Tester and J. B. Vander Sande, *Carbon*, 2004, **42**, 2295–2307.

26 J. Z. Wen, H. Richter, W. H. Green, J. B. Howard, M. Treska, P. M. Jardim and J. B. Vander Sande, *Journal of Materials Chemistry*, 2008, **18**, 1561.

27 R. L. Vander Wal, T. M. Ticich and V. E. Curtis, *Chemical Physics Letters*, 2000, **323**, 217–223.

28 Y. Li, X. Qiu, Y. Yin, F. Yang and Q. Fan, *Journal of Physics D: Applied Physics*, 2009, **42**, 155405.

29 C. Unrau, R. Axelbaum, P. Biswas and P. Fraundorf, *Proceedings of the Combustion Institute*, 2007, **31**, 1865–1872.

30 A. V. Saveliev, W. Merchan-Merchan and L. A. Kennedy, *Combustion and Flame*, 2003, **135**, 27–33.

31 S. S. Hou, D. H. Chung and T. H. Lin, *Carbon*, 2009, **47**, 938–947.

32 G. Mittal, V. Dhand, K. Y. Rhee, H.-J. Kim and D. H. Jung, *Carbon Letters*, 2015, **16**, 1–10.

33 P. Gopinath and J. Gore, *Combustion and Flame*, 2007, **151**, 542–550.

34 C. Hoecker, F. Smail, M. Bajada, M. Pick and A. Boies, *Carbon*, 2016, **96**, 116–124.

35 R. L. Vander Wal, G. M. Berger and L. J. Hall, *The Journal of Physical Chemistry B*, 2002, **106**, 3564–3567.

36 M. Poliak, A. Fomin, V. Tsionsky, S. Cheskis, I. Wlokas and I. Rahinov, *Physical chemistry chemical physics : PCCP*, 2014, **17**, 680–5.

37 R. L. Vander Wal, *Combustion and Flame*, 2002, **130**, 37–47.

38 R. L. Vander Wal and L. J. Hall, *Combustion and Flame*, 2002, **130**, 27–36.

39 S. Chaisitsak, J. Nukeaw and A. Tuantranont, *Diamond and Related Materials*, 2007, **16**, 1958–1966.

40 Y.-L. Li, L.-H. Zhang, X.-H. Zhong and A. H. Windle, *Nanotechnology*, 2007, **18**, 225604.

41 M. S. Motta, A. Moisala, I. A. Kinloch and A. H. Windle, *Journal of Nanoscience and Nanotechnology*, 2008, **8**, 2442–2449.

42 C. Hoecker, F. Smail, M. Pick and A. Boies, *Chemical Engineering Journal*, 2017, **314**, 388–395.

43 D. G. Goodwin, H. K. Moffat and R. L. Speth, *Cantera: An Object-Oriented Software Toolkit For Chemical Kinetics, Thermodynamics, And Transport Processes. Version 2.3.0*, 2017, `http://cantera.org/docs/sphinx/html/about.html`.

44 M. D. Smooke, *Journal of Computational Physics*, 1982, **48**, 72–105.

45 L. Slavov, M. V. Abrashev, T. Merodiiska, C. Gelev, R. E. Vandenberghe, I. Markova-Deneva and I. Nedkov, *Journal of Magnetism and Magnetic Materials*, 2010, **322**, 1904–1911.

46 D. L. A. de Faria, S. Venâncio Silva and M. T. de Oliveira, *Journal of Raman Spectroscopy*, 1997, **28**, 873–878.

47 G. Hou, D. Chauhan, V. Ng, C. Xu, Z. Yin, M. Paine, R. Su, V. Shanov, D. Mast, M. Schulz and Y. Liu, *Materials and Design*, 2017, **132**, 112–118.

48 S. L. H. Rebelo, A. Guedes, M. E. Szefczyk, M. Pereira and C. Freire, *Physical Chemistry Chemical Physics*, 2016, **18**, 12784–12796.

49 M. S. Dresselhaus, G. Dresselhaus, R. Saito and A. Jorio, *Physics Reports*, 2005, **409**, 47–99.

50 A. Sadezky, H. Muckenhuber, H. Grothe, R. Niessner and U. Pöschl, *Carbon*, 2005, **43**, 1731–1742.

51 A. C. Allwood, M. R. Walter and C. P. Marshall, *Vibrational Spectroscopy*, 2006, **41**, 190–197.

52 M. Knauer, M. Carrara, D. Rothe, R. Niessner and N. P. Ivleva, *Aerosol Science and Technology*, 2009, **43**, 1–8.